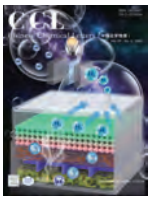
Chinese Chemical Letters 37 (2026) 111488

Contents lists available at ScienceDirect

Chinese Chemical Letters

journal homepage: www.elsevier.com/locate/cclet



Multifunctional FA-PDA@ICG-Bi_2Se_3 nanoplatform for targeted NIR and X-ray dual-modal imaging and photothermal therapy of cervical cancer

Zhong Du[a,1], Li-Jun Zhu[a,1], Jia-Bao Xiong[a], Yu-Xiang Gao[a], Ya-Qi Cui[b,c], Maierhaba Aili[d], Chen-Yang Chu[d], Chi Zhang[e], Gao-Fei Huang[c], Xue-Liang Zhang[c], Nuernisha Alifu[a,c,*], Biao Dong[b,c,*]

[a] *The Second Affiliated Hospital of Xinjiang Medical University, The Second School of Clinical Medicine, Xinjiang Medical University, Urumqi 830054, China*
[b] *State Key Laboratory on Integrated Optoelectronics College of Electronic Science and Engineering, Jilin University, Changchun 130012, China*
[c] *State Key Laboratory of Pathogenesis, Prevention and Treatment of High Incidence Diseases in Central Asia, School of Medical Engineering and Technology, Xinjiang Medical University, Urumqi 830011, China*
[d] *State Key Laboratory of Pathogenesis, Prevention, and Treatment of High Incidence Diseases in Central Asia, Department of Gynecology, The First Affiliated Hospital of Xinjiang Medical University, Urumqi 830054, China*
[e] *Department of Labor Hygiene and Environmental Hygiene, School of Public Health, Xinjiang Medical University, Urumqi 830054, China*

ARTICLE INFO

Article history:
Received 27 March 2025
Revised 16 June 2025
Accepted 18 June 2025
Available online 19 June 2025

Keywords:
NIR fluorescent imaging
Active targeting
Dual-modal imaging
Metastasis
Photothermal therapy

ABSTRACT

Cervical cancer remains a leading cause of cancer-related mortality in women, underscoring the urgent need for advanced diagnostic and therapeutic strategies. Current imaging techniques face significant limitations, including radiation exposure, high costs, and inadequate sensitivity for detecting early metastases, particularly in imaging and diagnosing tumor metastatic lesions. To overcome these challenges, we developed a multimodal imaging strategy that combined near-infrared fluorescence (NIRF, 750–1700 nm) imaging with X-ray imaging, with assistance of innovative nanomaterial to achieve precise tumor targeting and comprehensive diagnostic. Specifically, we synthesized a folate acid-functionalized polydopamine-modified ICG-Bi_2Se_3 nanocomposite (FA-PDA@ICG-Bi_2Se_3, FPBI), which integrated the complementary advantages of NIRF, X-ray, and computerized tomography imaging. The FPBI nanocomposite leveraged the targeting capability of folate acid for specific identification of cervical cancer lesions and metastatic lymph node. Furthermore, it demonstrated robust photothermal therapeutic efficacy under near-infrared (808 nm) excitation, achieving significant tumor ablation effects. This work provides an innovative nanoplatform based strategy for multimodal imaging, precise diagnosis, and targeted therapy of cervical cancer, paving the way for improved detection and management of metastatic lesions.

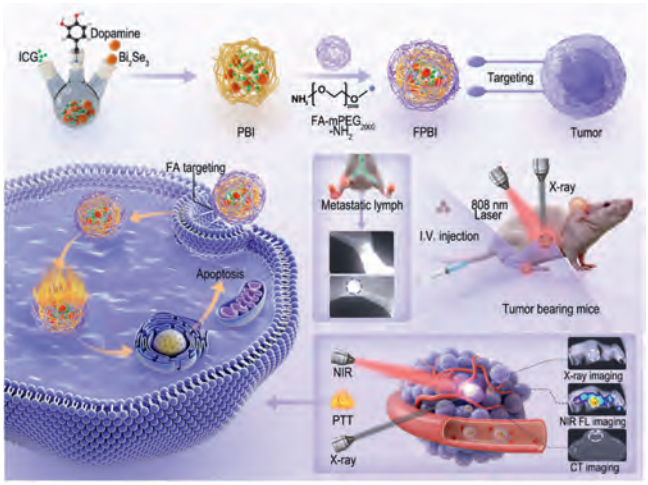
© 2026 Published by Elsevier B.V. on behalf of Chinese Chemical Society and Institute of Materia Medica, Chinese Academy of Medical Sciences.

Imaging examinations play a pivotal role during the diagnosis and treatment evaluation of cervical cancer [1]. Commonly used imaging techniques although play crucial roles in the biomedical detection and management, while still have been limited by radiation exposure, high costs, and patient-specific contraindications [2–4]. Thus, the safe and versatile imaging technologies are increasingly in huge demand [5,6]. Among them, near-infrared fluorescence (NIRF, 750–1700 nm) imaging has emerged as a promising molecular imaging technique, offering non-invasive detection of tissue-specific signals *via* fluorescent dyes excited by near-infrared lasers [7–9]. While NIRF shows potential in diagnosing tumors, inflammation, and vascular abnormalities [10–12], its clinical use is constrained by shallow penetration depth [13–15]. Among them, near-infrared II (NIR-II, 900–1700 nm) fluorescence imaging have exhibited advantages of high sensitivity, reduced scattering, and enhanced spatial resolution in deep tissue [16–18]. To achieve higher penetration depth as well as resolution and sensitivity, it is more favorable to combine NIRF imaging with X-ray imaging and computed tomography (CT). The multimodal imaging could help to achieve quick tumor localization, as well as providing accurate and comprehensive diagnostic solutions [19,20].

Another significant challenge lies in integrating NIR probes with other imaging modalities, which requires precise co-localized imaging to provide complementary and overlapping information

* Corresponding authors.
E-mail addresses: nens_xjmu@126.com (N. Alifu), dongb@jlu.edu.cn (B. Dong).
[1] These authors contributed equally to this work.

https://doi.org/10.1016/j.cclet.2025.111488
1001-8417/© 2026 Published by Elsevier B.V. on behalf of Chinese Chemical Society and Institute of Materia Medica, Chinese Academy of Medical Sciences.



Scheme 1. Illustration of FPBI NCs synthesis process, NIR multimodal bioimaging and PTT effect.

while enhancing the capabilities of multi-techniques [21]. Addressing this challenge demands breakthroughs in nanomaterial design. Bismuth-based nanomaterials have attracted attention for their high sensitivity to X-rays, which enables enhanced X-ray imaging [22]. Additionally, these materials respond to NIR light, allowing excitation to induce photothermal effects [23,24]. Currently, their application in NIRF imaging has been confirmed, and their potential in the NIR-II spectral region is equally enormous [25]. In addition, from the perspective of composite probe designing, the surface properties of Bi_2Se_3 nanomaterials make them highly suitable for functionalization with fluorescent molecules [26].

NIR-sensitive Bi_2Se_3 exhibits excellent photothermal therapeutic properties, making it highly attractive for designing integrated diagnostic and therapeutic strategies. However, challenges remain regarding their targeting specificity and biological safety under NIR light activation [27]. Designing polymeric network modification layers grown outward from the inorganic core is a key strategy for achieving integrated diagnostic and therapeutic systems [28]. Among various organic molecules, polydopamine (PDA) has received widespread attention. These characteristics stem from the abundance of cationic amino acids and catechol groups in PDA. In terms of optical performance, due to its energy level matching and strong adhesion, PDA can act as an "antenna molecule" to absorb near-infrared energy and transfer charges to inorganic materials, thereby improving overall photothermal performance [29]. As an organic network structure surrounding the inorganic core, PDA can further load NIR-II fluorescent molecules and targeting agents, making it an ideal platform for designing multimodal imaging and therapeutic systems. For instance, to enhance PDA's tumor-targeting ability, it can be functionalized with tumor-targeting molecules such as folic acid (FA) which achieves active targeting through its high affinity for folate receptors that are overexpressed in tumor tissues [30]. This strategy holds great promise for accurate tumor diagnosis and therapy, particularly for imaging metastatic lesions, and provides a foundation for developing efficient and safe multimodal imaging and therapeutic systems. In this study, as illustrated in the Scheme 1, we successfully developed a novel type of FA-PDA@ICG-Bi_2Se_3 (FPBI) nanocomposite (NCs). This composite leverages FA for precise navigation and active targeting of ICG and Bi_2Se_3, integrating multiple imaging modalities, including NIR-I, NIR-II, X-ray, and CT imaging, to harness their complementary advantages. The FPBI NCs demonstrated precise tumor localization and early detection of cervical cancer lymph node metastasis. PDA modification further enhanced biocompatibility, ensuring safety *in vivo*. Additionally, excitation with NIR light (808 nm) enabled targeted photothermal therapy (PTT), yielding significant therapeutic effects. These advancements provide a robust platform for multimodal imaging and precise diagnosis and treatment of cervical cancer.

Bi_2Se_3 nanosheets were synthesized and subsequently encapsulated in PDA *via* the self-polymerization of dopamine hydrochloride under alkaline conditions [31]. As shown in Fig. 1a, the resulting FPBI NCs exhibited a "rose-like" morphology under transmission electron microscopic (TEM) image. The particle size was around 150 nm (Fig. 1b). The particle size analysis of FPBI NCs in 1× phosphate buffered saline (PBS) solution were evaluated within 7 days (Fig. S1 in Supporting information). X-ray diffraction (XRD) analysis confirmed the presence of Bi_2Se_3 within the FPBI NCs (Fig. 1c). The ultraviolet-visible (UV–vis) absorption spectrum exhibited characteristic peaks at 500 nm (Bi_2Se_3) and 780 nm (ICG), validating the successful incorporation of both materials (Fig. 1d). According to absorption measurements, the loading dose of ICG in FPBI NCs was calculated to be 3.81 %, and the encapsulation efficiency was 91 %. Zeta potential analysis showed a surface charge shift from −25.06 mV to −19.44 mV after functionalization with FA-PEG-NH_2 (2000 kDa) and PDA, indicating successful modification (Fig. 1e). As depicted in Figs. 1f and j and Fig. S2 (Supporting information), XPS and EDS results revealed characteristic peaks for Bi, Se, S, and Cl, verifying the presence of these elements and the successful incorporation of both ICG and Bi_2Se_3. Figs. 1g and h illustrated changes in the binding energy of Bi and Se valence bonds in FPBI NCs compared to pure Bi_2Se_3. This electronically shared coordination enhances the internal structural stability of FPBI NCs and improves their physical properties [32]. By utilizing these unique charge transfer structures, strong metal electron transfer and the formation of interface sites can be promoted [33]. Fourier transform infrared spectrometer (FT-IR) spectral analysis (Fig. 1i) further supported these findings. Under 808 nm NIR excitation, FPBI NCs emitted fluorescence in the range of 820–840 nm (Fig. 1k). Compared to the fluorescence peak of free ICG, a slight redshift was observed. This shift likely resulted from PDA modification, which expanded the PDA shell's network structure. This structure transforms ICG to transition from a monomeric to an aggregated state within the NCs, altering the charge density distribution between interacting molecules. Furthermore, changes in the geometric configuration of ICG molecules may have affected the bandgap energy, contributing to the observed redshift [34]. In a 60 min photobleaching resistance experiment using an NIR-II fluorescence microscopic imaging system, FPBI NCs demonstrated higher fluorescence signal intensity than free ICG after 40 min of continuous irradiation (Fig. 1l). This suggests improved photostability, a critical factor for prolonged imaging applications.

The photothermal properties of FPBI NCs, ICG, Bi_2Se_3, PDA@ICG NCs and PDA@Bi_2Se_3 NCs were evaluated to assess the *in vitro* photothermal performance of FPBI NCs, as shown in Fig. S3a (Supporting information). The influence of concentration and laser power density on the properties of FPBI NCs was studied (Figs. S3b–d in Supporting information). The photothermal stability of FPBI NCs had been further demonstrated through five consecutive heating and cooling cycles. The photothermal conversion efficiency (PCE) of FPBI NCs was calculated to be 26.24 % (Figs. S3e and f in Supporting information). The cellular level imaging capabilities and photothermal therapeutic effects were further validated in HeLa cells and H8 cells (Figs. S4–S6 in Supporting information). FA functionalization enables more FPBI NCs to enter tumor cells, where NIR radiation activates FPBI NCs and converts NIR energy into thermal energy. The tumor targeting and PTT effects of FPBI NCs are key to achieving comprehensive diagnosis and treatment of cancer [35].

Based on the *ex vivo* fluorescence performance evaluation and cell level tracking localization ability of FPBI NCs, NIR-II fluores-

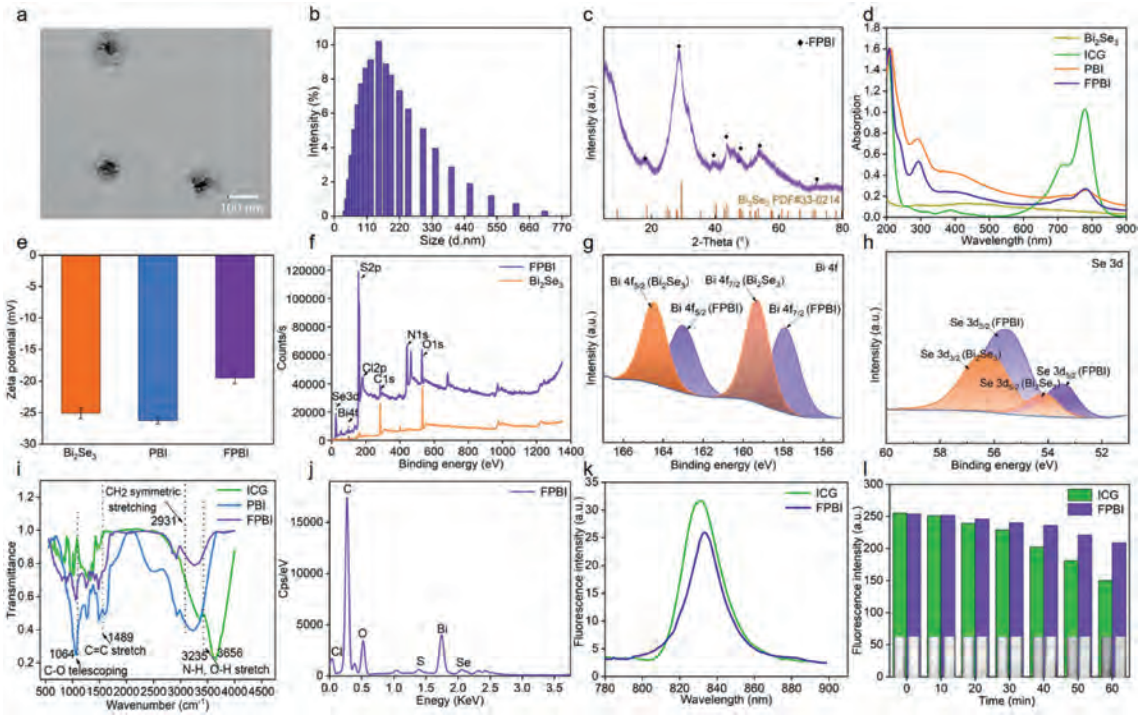


Fig. 1. Characterization of FPBI NCs. (a) Transmission electron microscopic image of FPBI NCs. (b) DLS analysis of FPBI NCs. (c) X-ray diffraction of FPBI NCs. (d) Absorption spectra of Bi_2Se_3, ICG, PBI NCs and FPBI NCs. (e) Zeta analysis of Bi_2Se_3, PBI NCs and FPBI NCs. Data were presented as mean ± standard deviation (SD) ($n = 3$). (f) X-ray photoelectron spectroscopy of Bi_2Se_3 and FPBI NCs. (g) The binding energy changes of Bi_2Se_3 and FPBI NCs at the Bi valence bond and (h) at the Se valence bond. (i) FT-IR of Bi_2Se_3, PBI NCs and FPBI NCs. (j) Energy dispersive spectrometer of FPBI NCs. (k) Fluorescence spectra of ICG and FPBI NCs. (l) Fluorescence intensity analysis of ICG and FPBI NCs (808 nm laser irradiation, 1 W/cm^2).

cence microscopic imaging system and IVIS spectral imaging systems were further utilized to analyze the NIR-II fluorescence capability. As shown in Figs. 2a and b, strong fluorescence signals were observed in the tumor site of tumor-bearing mice 24 h after tail vein injection of FPBI NCs, utilizing the NIR-II IVIS spectroscopic imaging system (808 nm laser, 500 mW/cm^2), indicated that the active targeting strategy utilizing FA as a target could mediate the internalization of more FPBI NCs by tumor cells, thereby achieving *in vivo* tumor localization and tracking. Through analyzing the full width at half maximum (FWHM) and signal to background ratio (SBR), NIR-II fluorescence images of cervical tumors with a high signal-to-noise ratio were acquired. The SBR value is 11.14 (Fig. S7 in Supporting information), indicating that FPBI NCs exhibit good imaging capabilities in NIR-II. Next, SOP TOP NIR-II FMMS was utilized to analyze the fluorescence imaging of microvessels in the tumor site of tumor-bearing mice. By adjusting the magnification of the objective lens, we carefully observed and clearly displayed the different collateral branches of the tumor's main blood vessels (Fig. 2c). As shown in Fig. 2d, the FWHM of the main blood vessels was analyzed, which also exhibited a high SBR.

Therefore, a lymph node (LN) tumor metastasis model was established to evaluate the recognition and tracking ability of FPBI NCs for early LN metastasis of tumors. FPBI NCs were injected into the tumor site of the foot pad, and after 30 min, utilizing the NIR-II IVIS spectroscopic imaging system (808 nm laser, 500 mW/cm^2), the accumulation of FPBI NCs significantly increased in mice with tumor infiltrating LN due to the specific binding of FA to FA receptors expressed on tumor cells (Fig. 2e). Finally, the primary tumor and excised LNs were subjected to diagnostic gold standard hematoxylin and eosin (H&E) staining. As shown in Fig. 2f, the boundary between normal tissue and LN tissue is clearly visible, and there is no residual lymph node at the edge of lymph node tissue, indicating complete resection of lymph node. Accurately identifying and dissecting sentinel LN is currently an important method in clinical cancer diagnosis. All animal experimental procedures have been approved by the Animal Experiment Ethics Committee of Xinjiang Medical University (No. IACUC-20,220,308–55).

Considering the X-ray absorption ability of Bi_2Se_3, further amplifying the advantages of NIRF imaging and increasing penetration depth, NIRF imaging was combined with X-ray imaging. As shown in Figs. 3a and b, after tail vein injection of FPBI NCs, strong fluorescence signals were observed at the tumor site in the FPBI NCs group mice at 24 h using the IVIS spectroscopic imaging system, compared to the ICG group mice. However, no significant fluorescence signals were observed in the tumor sites of the PBI NCs group mice without FA targets (Figs. S8 and S9 in Supporting information). ICP-MS analysis revealed the distribution of Bi and Se elements in organs and tumor sites of mice. More Bi and Se elements were concentrated at the tumor site, indicating that FPBI NCs could slow down the metabolic loss of Bi_2Se_3 *in vivo* under PDA encapsulation, allowing more Bi_2Se_3 to target the tumor site (Fig. 3c and Fig. S10 in Supporting information). The *in vivo* multimodal imaging performance of FPBI NCs was further evaluated. As shown in Figs. 3f and h, under NIR and X-ray irradiation, the superimposition of NIR and X-ray imaging effects was successfully achieved in cervical tumor-bearing mice. Strong fluorescence signals were observed from the tumor site, accompanied by changes in high-density shadows. With assistance of FPBI NCs, high spatial resolution in NIRF imaging was achieved, while also providing deep penetration *via* X-ray imaging. Integrating NIRF imaging and X-ray imaging into cancer diagnosis could further obtain more accurate information.

Based on the X-ray imaging performance of FPBI NCs, Micro-CT was utilized to further investigate the CT imaging effects of FPBI NCs both *in vitro* and *in vivo*. As illustrated in Figs. 3d and e, with increasing of FPBI NCs concentration, the Hounsfield unit (HU) value of CT imaging gradually rises, indicating greater absorption of X-rays. Furthermore, through *in vivo* CT imaging analysis,

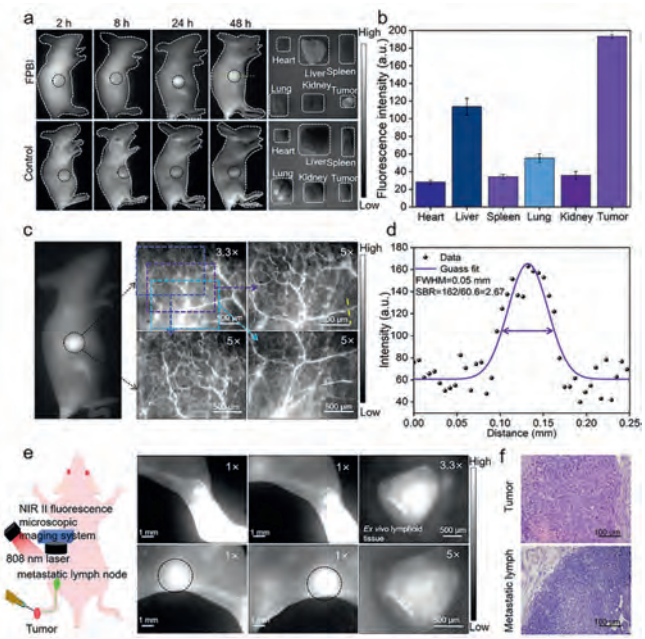


Fig. 2. *In vivo* NIR-II fluorescence imaging. (a) NIR-II fluorescence images of tumor site at different times after tail vein injection of 1× PBS and FPBI NCs, and corresponding fluorescence images of organs and tumors tissues in 48 h (808 nm laser, 500 mW/cm^2). (b) NIR-II fluorescence intensity analysis of organs and tumors at 48 h. Data were presented as mean ± SD ($n = 3$). (c) NIR-II fluorescence microscopic images of blood vessels in tumor sites. (d) SBR analysis of blood vessels in tumor sites. (e) NIR-II fluorescence images of metastatic sentinel lymph nodes. (f) H&E stained sections of primary tumor and metastatic lymph nodes.

it was observed that compared to the control group, tumor mice injected with FPBI NCs exhibited more pronounced high-density shadows at the tumor site (Fig. 3g), and the HU value was significantly higher than that of the control group (Fig. 3i). In the early detection of tumors, intraoperative navigation, and disease diagnosis and treatment in the future, this dual-mode imaging technology is expected to provide biomedical researchers with more accurate and comprehensive diagnostic basis, thereby improving treatment effectiveness and benefiting patients.

As depicted in Fig. S11 (Supporting information), a potent NIR-I fluorescence signal persisted *in vivo* for up to 48 h, indicating a prolonged metabolic duration. And major organs (heart, liver, spleen, lungs, and kidneys) were collected for *in vitro* fluorescence intensity analysis (Fig. S12 in Supporting information). The *ex vivo* imaging of the organs further corroborated the pronounced fluorescence signal originating from the liver. To further assess the fluorescence stability of FPBI NCs in the *in vivo* blood circulation (Figs. S13 and S14 in Supporting information). After 24 h of blood circulation and metabolism, the fluorescence signals from FPBI NCs in mouse blood had decreased by <50 % compared to the fluorescence signals after injection for 2 h (Figs. S15 and S16 in Supporting information), indicating that FPBI NCs, with the assistance of PDA and Bi_2Se_3, could slow down the fluorescence quenching of ICG and improve its fluorescence stability.

The *in vivo* antitumor efficiency of FPBI NCs was evaluated. After 24 h post-injection, the tumor site was irradiated with an 808 nm NIR laser (1 W/cm^2) for 10 min, and the temperature change of the irradiated site was observed using a thermal imaging instrument (Figs. 4a and b). The results of *in vivo* photothermal imaging experiments showed that under 808 nm laser irradiation, FPBI NCs injected through the tail vein absorbed light energy and converted it into heat energy, causing the temperature of the mouse tumor site to rise to 53.9 °C, which meets the conditions for effective tumor PTT [36,37]. Further research was conducted on the *in vivo* PTT effect of 808 nm laser on cervical tumor-bearing mice. After 14 days of treatment and observation, mice were euthanized and tumors and important organs were removed (Fig. 4c). The weight comparison analysis of tumors from different groups showed that the tumor quality of the FPBI NCs+laser group was significantly lower than that of the other three groups (Fig. 4d).

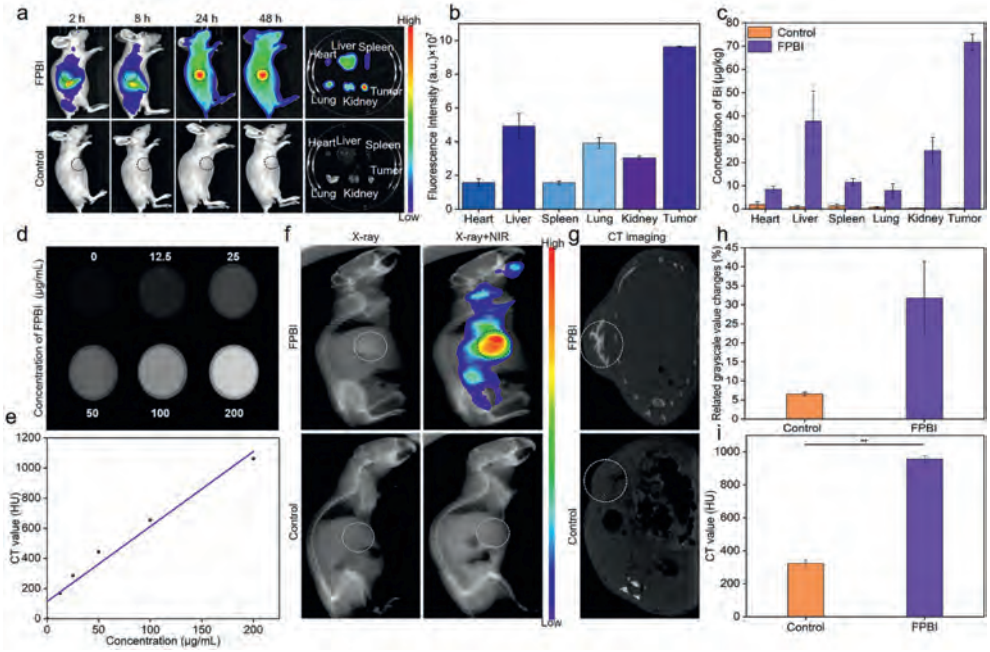


Fig. 3. *In vivo* multimodal imaging. (a) NIR-I fluorescence images of tumor sites at different times after tail vein injection of 1× PBS and FPBI NCs, corresponding fluorescence images of organs and tumors in 48 h. (b) Fluorescence intensity analysis of organs and tumors at 48 h. (c) ICP-MS analysis of Bi content in organs and tumors at 48 h. (d) *In vitro* CT images of FPBI NCs dispersion in different concentrations. (e) CT value as a function of concentration of FPBI NCs, slope obtained by linear fitting of the experimental data is the HU values of FPBI NCs. (f) Dual-modal *in vivo* imaging integrating X-ray imaging and NIR-I fluorescence imaging and (h) Changes in grayscale values related to tumor sites. (g) CT imaging of the tumor sites and (i) HU values of the tumor sites. Data were presented as mean ± SD ($n = 3$).

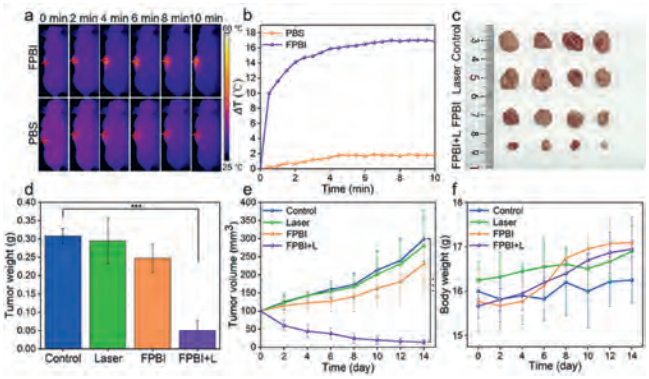


Fig. 4. (a) Thermal images of PBS and FPBI NCs at tumor sites (1 mg/kg) under irradiation of 808 nm laser at 1 W/cm^2 for 10 min. (b) Temperature rise curves of PBS and FPBI NCs at tumor sites. (c) Tumor images after different interventions. (d) Tumor weight from different interventions. (e) Tumor volume from different interventions. (f) Body weight from different interventions. Data were presented as the mean ± SD ($n = 4$). $^{***}P < 0.001$.

During the entire observation period, the tumor growth of the FPBI NCs + laser group showed significant inhibition and ablation effects (Fig. 4e), the tumor inhibition rate was 86.1 %. During the observation period, there was no significant change in the weight of the mice (Fig. 4f), after the observation period, the main organs and tumor tissues of the mice were removed and subjected to H&E staining section observation. No obvious organ inflammation or damage was found in the sections (Fig. S17 in Supporting information). A series of biosafety experiments were designed here to evaluate the biosafety of FPBI NCs (Figs. S18–S20 in Supporting information). FPBI NCs demonstrated good biocompatibility and *in vivo* clearance. Hemolysis studies were conducted (Fig. S21 in Supporting information), FPBI NCs did not exhibit significant hemolysis. The hemolysis rate tested at a concentration of 100 μg/mL was 3.8 %, these findings validated the potential applications of FPBI NCs in bioimaging and therapy, providing a biosafety foundation for future clinical translation.

In summary, a novel type of multifunctional, diagnostic therapeutic integrated nanocomposite material was successfully designed and developed for the combination of NIRF imaging with X-ray imaging and PTT for cervical cancer. Leveraging the targeting capabilities of FA, PDA encapsulated the NIR fluorescent probe ICG and CT enhancer Bi_2Se_3, enabling *in vivo* targeted tracking and localization of cervical tumors. Furthermore, NIR-II fluorescence imaging facilitated the observation of tumor microvessels, achieving a high SBR and deep-tissue penetration capability for tumor micro tissues. Additionally, it can perform non-invasive, real-time, and accurate tracking and localization of cervical cancer LN metastasis lesions. This study offers a novel preclinical trial strategy and approach for the diagnosis and treatment of cervical cancer, encompassing the integration of multimodal imaging techniques, monitoring of early metastasis, and treatment methods for cervical cancer.

Declaration of competing interest

The authors declare that they have no known competing financial interests or personal relationships that could have appeared to influence the work reported in this paper.

CRediT authorship contribution statement

Zhong Du: Writing – original draft, Software, Methodology, Investigation. **Li-Jun Zhu:** Writing – original draft, Software, Methodology, Conceptualization. **Jia-Bao Xiong:** Writing – review & editing. **Yu-Xiang Gao:** Software. **Ya-Qi Cui:** Resources. **Maierhaba Aili:** Methodology. **Chen-Yang Chu:** Resources. **Chi Zhang:** Validation. **Gao-Fei Huang:** Data curation. **Xue-Liang Zhang:** Funding acquisition. **Nuernisha Alifu:** Writing – review & editing, Supervision, Funding acquisition. **Biao Dong:** Writing – review & editing, Supervision, Funding acquisition.

Acknowledgments

This work was supported by Xinjiang Uygur Autonomous Region Natural Science Foundation Youth Top Talent Project (No. 2022TSYCCX0032). The Tianchi Talent Project (No. 03010511). Xinjiang Uygur Autonomous Region Regional Collaborative Innovation Special Science and Technology Assistance Program (No. 2022E02130), Xinjiang Uygur Autonomous Region Natural Science Foundation Key Project (No. 2022D01D40), Outstanding Youth Project (No. 2023D01E06) and Youth Science Fund (No. 2022D01C715), National Science Foundation of China (Nos. 82073475, 52250007, 62035011, 82202220 and 82060326), State Key Laboratory of Pathogenesis, Prevention and treatment of High Incident Diseases in central Asia (No. SKL-HIDCA-2024-GJ9).

Supplementary materials

Supplementary material associated with this article can be found, in the online version, at doi:10.1016/j.cclet.2025.111488.

References

[1] U. Mahantshetty, R. Poetter, S. Beriwal, et al., Radiother. Oncol. 160 (2021) 273–284.
[2] M. Saleh, M. Virarkar, S. Javadi, et al., AJR Am. J. Roentgenol. 214 (2020) 1182–1195.
[3] E. Burian, B. Palla, N. Callahan, et al., Eur. J. Nucl. Med. Mol. ImAging 49 (2022) 3870–3877.
[4] J. Chu, X. Yu, G. Jiang, et al., Microb. Biotechnol. 17 (2024) e14474.
[5] K. Ravina, L. Lin, C.Y. Liu, et al., Neurosurgery 87 (2020) 11–24.
[6] H. Li, P. Li, J. Zhang, et al., Nanoscale 16 (2024) 21697–21730.
[7] H. Shang, Y. Yang, B. Xue, et al., Chin. Chem. Lett. 36 (2025) 110511.
[8] X. Lv, X. Ran, Y. Zhao, et al., Chin. Chem. Lett. 36 (2025) 110027.
[9] A. Yang, Y. Wang, Q. Feng, et al., Adv. Healthc. Mater. 13 (2024) e2302687.
[10] Y. Xu, B. Chen, D. Su, et al., ACS Appl. Mater. Interfaces 15 (2023) 56314–56327.
[11] M. Sun, M. Li, M. Hu, et al., ACS Nano 18 (2024) 33907–33921.
[12] J. Wan, X. Zhang, D. Tang, T. Liu, H. Xiao, Adv. Mater. 35 (2023) e2209799.
[13] J. Hu, L. Yan, Z. Cao, et al., Adv. Sci. 11 (2024) e2407196.
[14] H. Wu, P. Chen, X. Zhan, et al., Adv. Mater. 36 (2024) e2310571.
[15] S. Zhang, H. Yuan, S. Sun, et al., Adv. Sci. 10 (2023) e2207651.
[16] B. Huang, T. Tang, F. Liu, et al., Chin. Chem. Lett. 35 (2024) 109694.
[17] M. Yang, H. Gong, D. Yang, et al., Chin. Chem. Lett. 35 (2024) 108468.
[18] Y. Jiang, L. Wang, B. Hu, et al., Adv. Healthc. Mater. 13 (2024) e2402828.
[19] M. Li, Y. Wang, T. Li, et al., Acta Biomater. 155 (2023) 564–574.
[20] D. Xu, J. Ge, Y. An, et al., Small 19 (2023) e2300859.
[21] R.S. Das, D. Maiti, S. Kar, et al., J. Am. Chem. Soc. 145 (2023) 20451–20461.
[22] S. Wu, X. Meng, X. Jiang, et al., Adv. Sci. 8 (2021) e2002548.
[23] Q. Wang, J. Liu, D. Chen, et al., Adv. Healthc. Mater. 12 (2023) e2202622.
[24] L. Yang, Z. Zhao, B. Tian, et al., Nat. Commun. 15 (2024) 7499.
[25] N. Meng, P. Xu, C. Wen, et al., J. Colloid Interface Sci. 644 (2023) 437–453.
[26] D. Wen, L. Dong, K. Li, et al., ACS Appl. Mater. Interfaces. 13 (2021) 48378–48385.
[27] Y. Song, J. Wang, L. Liu, et al., Mol. Pharm. 15 (2018) 1941–1953.
[28] Y. Li, C. Aparicio, PLoS One 8 (2013) e76782.
[29] S. Cheng, M. Qi, W. Li, et al., Adv. Healthc. Mater. 12 (2023) e2202652.
[30] S. Ye, W. Zhang, Y. Shen, et al., Macromol. Rapid. Commun. 44 (2023) e2300298.
[31] Z. Du, R. Ma, S. Chen, et al., Nanoscale Adv. 4 (2022) 4016–4024.
[32] Y. Zhang, T. Bian, R. Jiang, et al., J. Hazard. Mater. 407 (2021) 124347.
[33] Y. Liu, J. Ding, F. Li, et al., Adv. Mater. 35 (2023) e2207114.
[34] R.A. Hauyon, D. Fuentealba, N. Pizarro, et al., Polymers 15 (2022) 67.
[35] H. Wang, S. Lin, S. Wang, et al., Nano Lett. 22 (2022) 6516–6522.
[36] C.F. Cuadrado, K.J. Lagos, M.D. Stringasci, V.S. Bagnato, M.P. Romero, Photodiagnosis. Photodyn. Ther. 50 (2024) 104387.
[37] Y. Dong, S. Dong, C. Yu, et al., Sci. Adv. 9 (2023) eadi9980.